3D interfaces enhance nanolaminate strength and deformability in multiple loading orientations

Justin Y. Cheng [a], Jiaxiang Wang [b], Youxing Chen [c], Shuozhi Xu [d], Javier G. Barriocanal [e], J. Kevin Baldwin [f], Irene J. Beyerlein [b,g], Nathan A. Mara [a,*]

[a] *Department of Chemical Engineering and Materials Science, University of Minnesota Twin Cities, Minneapolis, MN 55455, USA*
[b] *Department of Mechanical Engineering, University of California, Santa Barbara, CA 93106, USA*
[c] *Mechanical Engineering and Engineering Science, University of North Carolina, Charlotte, NC 28223, USA*
[d] *School of Aerospace and Mechanical Engineering, University of Oklahoma, Norman, OK 73019, USA*
[e] *Characterization Facility, University of Minnesota Twin Cities, Minneapolis, MN 55455, USA*
[f] *Center for Integrated Nanotechnologies, Los Alamos National Laboratory, Los Alamos, NM 87545, USA*
[g] *Materials Department, University of California, Santa Barbara, CA 93106, USA*

ARTICLE INFO

ABSTRACT

3D interfaces are a new type of interface containing nanoscale crystallographic, structural, and chemical heterogeneities in all spatial dimensions. Recently, 3D interfaces have been shown to enhance strength and deformability simultaneously by frustrating shear instability under layer-normal micropillar compression in Cu/ Nb nanolaminates. However, quantification of deformed microstructure and effects of loading orientation were not explored in that work. Here, we address these shortcomings by performing *post mortem* TEM characterization of micropillars compressed at normal and 45° inclination to layers. We find high strength and deformability in both loading geometries and show that 3D interfaces enhance mechanical behavior under multiple loading orientations. In layer-normal compression, *post mortem* characterization allows for quantification of key quantities correlating well to the severity of shear localization across nanolaminates with different layer thickness and interface type. In 45° compression, TEM results demonstrated no strong plastic instability. This motivated analytical computation of Schmid factors and simulation of slip system activity via crystal plasticity finite element modeling (CPFE). The CPFE model demonstrates that most slip activity occurs non-parallel to layers, indicating that dislocation-3D interface interactions must mediate the observed mechanical behavior of micropillars. This work lays the foundation for further study of 3D interface-driven deformation physics in nanostructured alloys.

1. Introduction

Nanostructured alloys are of great interest for structural applications due to their impressive strength across a wide range of metals [1]. However, it is well known that they suffer from limited ductility and low work hardenability due to shear instability or fracture during deformation [2]. This "strength-ductility tradeoff" [3] can be mitigated by methods such as introduction of tailored grain size gradients, engineered grain boundaries, second phases, or interphase interfaces with controlled structure [4,5]. Examples of nanostructured alloys with interface content and structure successfully controlled to improve mechanical properties include nanocrystalline(nc) such as Cu-Zr with

amorphous intergranular films [6], Al-Mg with doped grain boundaries [7], and nanotwinned pure Cu [8] and Al alloys [9]. Single-phase or interphase interfaces can play a great role in the deformation of nanostructured materials since a large fraction of material lies near grain and/or interphase boundaries. Whether interfaces themselves shear to contribute to plastic deformation [12] or impede dislocation motion [13], their atomic-level structure can influence how much interfaces can enhance mechanical properties [5]. Recent work has shown that single-phase nanostructured alloys containing copious coherent twin boundaries possess enhanced strength compared to those without [14–16]. These stable low-energy boundaries help both to block dislocation motion and enhance dislocation storage in crystals abutting the

---

* Corresponding author.
E-mail address: mara@umn.edu (N.A. Mara).

twin lamellae [17], bestowing high strength and ductility even at nanoscale lamellar spacing. The strategy of interfacial microstructure control can also be used in multiphase materials at heterophase interfaces, which are the focus of this work. Such interfaces are found in nanostructured alloys with potential for engineering usage such as oxide dispersion strengthened austenitic steels [10] and twinning-induced plasticity steels [11].

In heterophase materials certain low energy, stable incoherent interface structures are favored by thermodynamics, and their relation to strengthening has been explored extensively in many composite systems. Early studies focused on Cu/X multilayers, where X=Nb, Ni, or Cr [18,19], but the literature has recently expanded to a wide variety of bimetallic combinations, such as Al/Nb, Cu/Ni, Cu/Zr, Mg/Nb, and Mg/Ti [20]. These represent face-centered cubic (FCC)/body-centered cubic (BCC), FCC/FCC, FCC/hexagonal close-packed(HCP), HCP/BCC, and HCP/HCP systems, respectively. More exotic nanolaminates have also been made, such as Cu/HEA nanolaminates [21], Cu-amorphous CuZr nanolaminates [22], pseudomorphic BCC Mg/Nb nanolaminates [23], and Cu/Nb with amorphous interlayers [24]. Among the biphase combinations, the Cu/Nb system is the most widely studied [25–33]. Cu/Nb is uniquely suited for such work due to the immiscibility of its constituent phases and predominant Nishiyama-Wassermann (N-W) and Kurdjumov-Sachs (K-S) type interfaces [26]. Cu/Nb nanolaminates have been made via physical vapor deposition (PVD) [34] and accumulative roll bonding (ARB) [25,35]. These synthesis methods produce material dominated by K-S and N-W interfacial orientation relationships joined along different crystallographic planes. The pure phases are joined at the {111}Cu/{110} Nb planes in the PVD material, but along mutual {112} planes in the ARB case. Moreover, PVD Cu-Nb interfaces are atomically flat, while ARB Cu-Nb interfaces have a serrated morphology [25]. The PVD and ARB Cu/Nb nanolaminates exhibit noticeable differences in strength, deformability, and failure mode between materials [36].

Atomistic simulations have suggested that the interfacial atomic configuration controls deformation at the nanoscale, where interfaces participate in a substantial fraction of unit deformation events. PVD Cu/Nb interfaces have a low shear strength of <0.8 GPa and deform by sliding under any applied in-plane shear stress. In contrast, ARB Cu/Nb interfaces have a high shear strength of >1.5 GPa and may slide or emit dislocations depending on the shear direction [37,38]. Nanolaminates with low interfacial shear strengths allow glide dislocation cores to easily spread in the interface, restricting their propagation [36]. Thus, low interfacial shear strength PVD Cu/Nb interfaces tend to pose greater obstacles to dislocation transmission compared to those of high shear strength ARB Cu/Nb interfaces. MD simulations of confined layer slip show that high shear strength ARB interfaces with protruding misfit dislocations offer greater glide resistance and promote jerky glide compared to coherent twin interfaces [39]. Dislocation nucleation is also strongly affected by interface structure [25,35]. The unit defect-interface interactions associated with each interface structure ultimately determine the degree and form of plastic instability that occurs in the material during mechanical testing [13,40–43]. Previous work showed that micropillars of PVD Cu/Nb exhibited flow instability by formation of a single shear band traversing the pillar when compressed. Shear band formation initiated after significant lattice rotation and was subsequently mediated by interface sliding for layer thicknesses below a few tens of nanometers [27,44]. In contrast, similar tests in 18 nm layer thickness ARB Cu/Nb showed many small shear bands along the length of the pillar [36,45]. Clearly, different interface structures bestow different mechanical behaviors that ultimately determine the extent of uniform plastic deformation. If interface structure can be controlled repeatably in nanocrystalline systems, then mechanical behavior can be manipulated to optimize material performance.

Recently, we controlled interface structure in PVD Cu/Nb by introducing three-dimensional (3D) heterophase interfaces to form "3D Cu/Nb" [46,47]. 3D interfaces are interphase boundaries that are chemically, crystallographically, and/or topologically heterogeneous in all

spatial dimensions [46,48]. In contrast, the PVD and ARB Cu/Nb studied in the literature mentioned above have atomically sharp 2D interfaces in the interface normal direction and comprise 2D Cu/Nb. We have shown previously that 3D interfaces strengthen Cu/Nb over their 2D counterparts without sacrificing deformability [46] and simultaneously enhance both strength and deformability with reduced layer thickness h [47], suggesting a size effect dependent on relative scale between h and interface thickness h'. Prior work focused on 3D interfaces with thickness h'= 10 nm. Results from a mesoscale discrete dislocation dynamics technique called phase field dislocation dynamics (PFDD) suggested that with all else being the same, thicker 3D interfaces pose higher resistance to slip transfer. 3D interface strengthening was found to be stronger when the dislocation was extended into a lead and trailing dislocation compared to when it was compact [49,50]. Using the same PFDD technique for modeling pileups against the interface, it was observed that when h' was large enough compared to the pileup size in the adjoining pure layer, slip on a single slip system was attenuated, activating secondary slip and frustrating shear band formation across 3D interfaces [51].

Despite insights from previous work, the contribution of 3D interfaces to deformation is not fully explored. Post-deformation microstructures in 3D Cu/Nb were not quantified and tests were performed in one loading state. To address these issues, we study the nature of plastic instability in Cu/Nb as a function of atomic interface structure and loading orientation using new work and previous literature results. Previous work shows that 2D PVD interfaces can slide when compressed at a 45° angle, or during shear instability formation after the onset of layer rotation in 2D interfaces fabricated via PVD and ARB [27,45,52, 53]. In this work, we probe the mechanical response of 3D interfaces under different loading conditions, where 10–10 Cu/Nb micropillars are compressed either perpendicular or at 45° to the Cu and Nb layers. 3D interface contribution to deformation is analyzed in terms of shear localization intensity and local material rotation. Quantification of post-deformation microstructures prompts an investigation of slip system activity involving crystal plasticity finite element (CPFE) simulation. This allows for development of a dislocation-based model explaining superior deformability and strength in 3D Cu/Nb under multiple loading orientations.

2. Experimental

We fabricated 3D Cu/Nb samples using direct current (DC) magnetron sputtering. 10-micron thick films were deposited on pieces of (100) Si substrate with a native oxide at room temperature on a rotating stage. The base pressure was $1*10^{-6}$ Torr, and Ar working gas was flowed in at 3 mTorr during deposition. Pure Cu and Nb were deposited at a rate of 3 Å/s. 3D interfaces were introduced between pure Cu and Nb layers by gradually ramping Cu and Nb target powers in opposite directions between deposition of pure layers as done in prior work [46,51]. For this work, nominal pure layer thickness h was 10 nm and 3D interface thickness h' was also 10 nm. We refer to this material as 10–10 3D Cu/Nb.
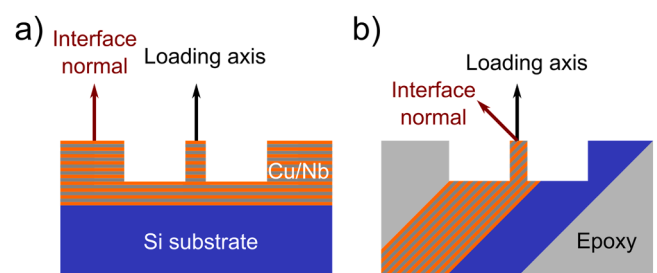

Fig. 1. Schematic of sample and loading orientation in a) normal and b) 45° compression.

Micropillars were made from deposited films with two compression orientations as shown in Fig. 1. Normal compression refers to the angle of the compression axis relative to layer- and interface- parallel directions. The other set of pillars, which we call 45° pillars, were oriented such that the compression axis was at a 45° inclination to the layers. The 45° pillars were made by mounting substrate-supported thin film samples between two pieces of an SEM stub cut at 45° and performing metallographic polishing. After casting the stub-film combination in a thin layer of cold mounting epoxy, the sample was ground using SiC sandpaper from 400 to 1200 grit, polished using diamond lapping films from 9- to 1-micron particle size and alumina suspension with 0.3-micron particles, and finally vibratory polished using colloidal silica. Micropillars were made using a FEI Helios FIB/SEM by milling annular regions of decreasing inner and outer radius at an accelerating voltage of 30 keV and currents ranging from 65 nA down to 90 pA. Pillar dimensions were nominally 3 μm in diameter and 6 μm in height to achieve an aspect ratio of 2. This was to ensure that pillar aspect ratio fell inside the ideal range of 2–3 to avoid buckling while allowing any shear instabilities to traverse the width of the pillars [54].

Micropillar compression was performed *in situ* using a Bruker Hysitron PI 88 in a FEI Quanta 200 3D FIB/SEM. Pillars were compressed at an initial strain rate of 10^{-3}/s to engineering strains of 0.18 and 0.36. Deformed pillars were imaged by SEM and cut into electron transparent lamellae in the FEI Helios FIB/SEM. Conventional TEM (CTEM), high-resolution TEM (HRTEM), high angle annular dark field scanning TEM (HAADF-STEM) and scanning TEM energy dispersive spectroscopy (STEM-EDS) were conducted on FIB-thinned lamellae in a Thermo Fisher Talos F200X at 200 keV.

The crystallographic texture of 10–10 Cu/Nb was measured using 2D XRD. X-ray pole figure measurements were completed using a Bruker D8 Discover equipped with a graphite-monochromated Co K_α source and a VÅNTEC-500 two-dimensional x-ray detector with 0.04° angle resolution at 20 cm sample-to-detector distance. φ scans were completed from 0–360° at various 2θ, ω, and ψ at 20 seconds per frame to achieve good coverage of Cu (111), (200), (220) and Nb (110), (200), (112) pole figures. The goniometer angles used in this experiment are summarized in Table 1. 2D XRD frames were analyzed using Bruker GADDS to process sets of frames into pole figures. These pole figures were imported into MTEX [55] for further processing. The first step in MTEX was to interpolate missing data points and remove Si (100) substrate peaks. Si

Table 1
A summary of goniometer angles used in X-ray pole figure measurements for this work. Sets of φ scans are grouped by the pole figures they were optimized for.

Pole figures	2θ(°)	ω(°)	ψ(°)	Δφ(°)
Cu (111) Nb (110)	47	25	20	5
Cu (111) Nb (110)	47	25	55	2.5
Cu (111) Nb (110)	47	25	85	2.5
Cu (200) Nb (200)	62.5	32.5	15	5
Cu (200) Nb (200)	62.5	32.5	45	2.5
Cu (200) Nb (200)	62.5	32.5	75	2.5
Cu (200) Nb (200)	62.5	32.5	85	2.5
Cu (220) Nb (112)	86.5	44	10	5
Cu (220) Nb (112)	86.5	44	30	2.5
Cu (220) Nb (112)	86.5	44	50	2.5
Cu (220) Nb (112)	86.5	44	72	2.5
Cu (220) Nb (112)	86.5	44	85	2.5

Table 2
A summary of average Cu and Nb layer thickness, as well as 3D interface thickness. *h'* was measured separately for 3D interfaces deposited on Cu and Nb layers to probe differences in growth for interfaces deposited on different layers. Sample size is 6 layers for h_{Cu} and 5 layers/interfaces for all other thicknesses.

	Average(nm)	Std. Dev. (nm)
h_{Cu}	10.4	0.6
h_{Nb}	9.6	0.4
h' (3D interface on Cu)	11.0	0.5
h'(3D interface on Nb)	10.8	0.3
Bilayer ($h_{Cu} + h_{Nb} + 2h'$)	41.8	0.4

substrate peaks were removed by deleting outlier data points in experimentally measured pole figures – these peaks were much more intense than the maximum signal from Cu or Nb in the sputtered film. Interpolation was done using the interp function in MTEX over a grid from 0–90° in α and 0–360° in β with a step size of 3° in both coordinates. The scaling factor associated with polarization, background, and detector factors was determined experimentally by measuring pole figures using APS 10-micron Cu powder sprinkled onto a thin layer of vacuum grease. These scaling factor pole figures were then divided pointwise out of interpolated Cu/Nb pole figures to produce quantitative pole figures [56]. Then, pole figures were normalized in MTEX. Lastly, orientation distribution functions (ODF) were fit to pole figures at a resolution of 5° and using a de Vallee Poussin kernel width of 5° for CPFE modeling purposes. Pole figures presented in this work are projected from these ODFs.

3. Results

### 3.1. Microstructure of undeformed 10–10 Cu/Nb

Fig. 2 presents the microstructure of undeformed 10–10 Cu/Nb far below the gauge length of the layer-normal compression pillar that serves as the reference microstructure in this work. Fig. 2(a and b) shows that one set of Cu {111} and Nb {110} planes are oriented parallel to the layer direction. Both Nb [111] and [001] zone axis patterns are visible, consistent with the Kurdjumov-Sachs and Nishiyama-Wasserman orientation relationships, respectively [34]. The HAADF image and diffraction pattern show that Cu and Nb lattices are initially oriented with predominantly Cu {111} and Nb {110} parallel to the interfaces. This is the same texture reported for PVD 2D Cu/Nb [35]. Fig. 2(c and d) shows a STEM-EDS map and a composition profile taken perpendicular to layers to measure actual layer thickness. 3D interfaces grown on Cu are distinguished from those grown on Nb since different epitaxy in these two cases could lead to microstructural differences. The measured thicknesses are summarized in Table 2. These results show that Cu, Nb, and 3D interface thicknesses are close to the nominal value of 10 nm. X-ray texture measurement is presented in Fig. 3. 10–10 Cu/Nb has a fiber texture with Cu {111} and Nb{110} planes aligned along the growth direction. These textures are consistent with the Kurdjumov-Sachs and Nishiyama-Wassermann orientation relationships found in TEM from Fig. 2.

3.2. Deformation in layer-normal and 45° compression

Fig. 4 shows representative stress-strain curves taken from normal and 45° compression pillars along with post-deformation microstructures characterized using TEM. The instantaneous cross-sectional area for stress calculation is determined with a tapered pillar model [51]. This model is used until the tapered pillar deforms into a right cylinder. The cross-sectional area at this point is used to calculate engineering stress for higher strains. Strains presented are engineering, with the gage length of each pillar determined by comparing video frames from *in situ* compression footage at the beginning and end of testing. The bottom of the gage length is defined by the bottom-most point on the pillar that
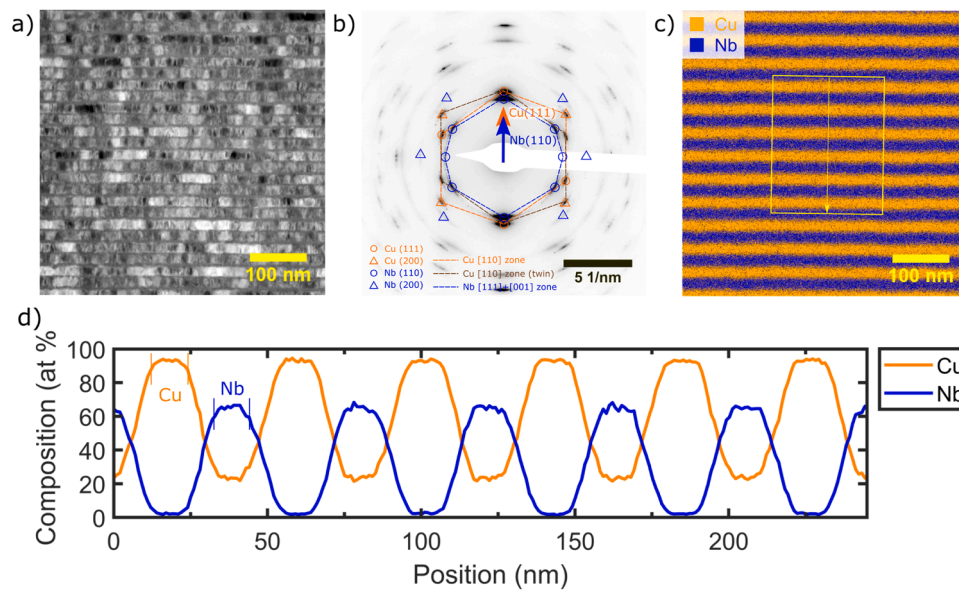
Fig. 2. a) HAADF-STEM image of undeformed 10–10 Cu/Nb. b) Grayscale-inverted SAD diffraction pattern from near the region shown in a) showing that Cu (111) and Nb (110) planes are parallel to layer directions. Note that the orientation between a) and b) does not change – a direction indicated in reciprocal space in b) is aligned with the same direction in real space in a). All further diffraction patterns in this work will be grayscale inverted. c) depicts a STEM-EDS map of region a) with Cu in orange and Nb in blue. d) depicts an elemental profile taken from c) along the direction of the yellow arrow and averaged along the width of the box encompassing that arrow. The layer and interface thicknesses taken from this profile are summarized in Table 2. Note that Nb layers appear impure due to the redeposition of more mobile Cu during FIB preparation of TEM specimens [57].
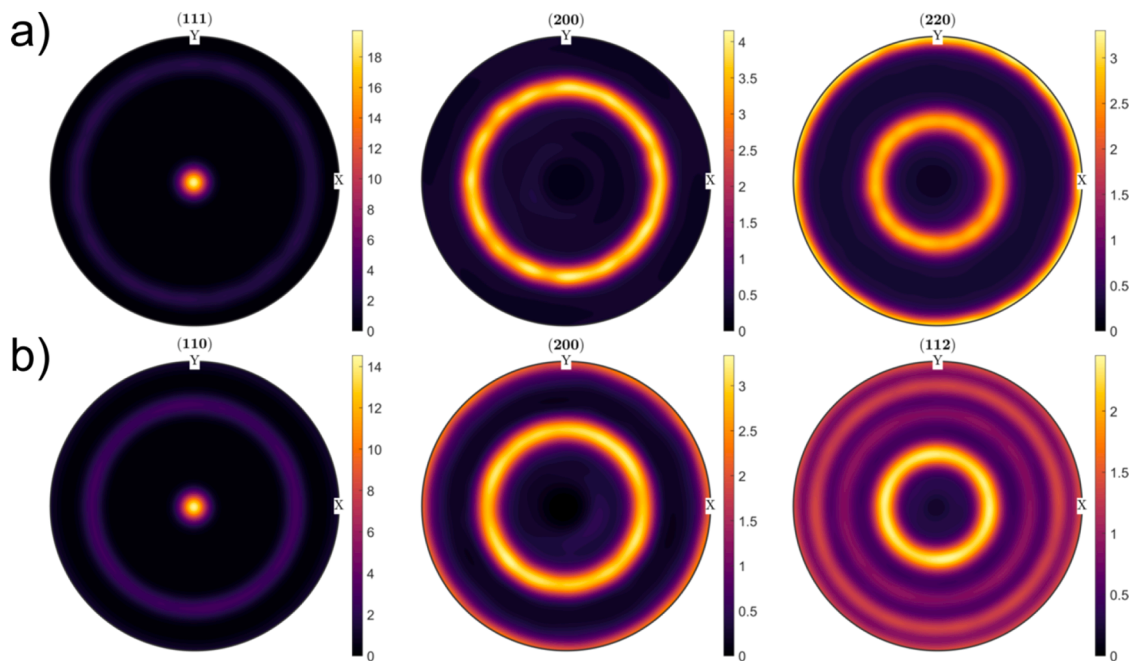

Fig. 3. Pole figures of a) Cu and b) Nb in 10–10 Cu/Nb, made by projecting ODFs fit to X-ray data. Both sets of pole figures demonstrate a fiber texture.

exhibits a measurable change in width during testing. An example of the gage length determination process can be found in Fig. S1. Three pillars were compressed for each loading state whose stress strain curves can be found in Fig. S2. The yield stress is taken from where the stress strain curve deviates from the initial linear portion by 5%. For layer-normal compression pillars, the yield stress is 2080±170 MPa and for 45° pillars it is a substantially lower 820±53 MPa. This constitutes a yield stress ratio of 2.53:1 between normal and 45° compression. For reference, a yield stress ratio of 3.00:1 between normal and 45° compression was found for 2D interface Mg/Nb nanolaminates of comparable h in

other work [53]. It should be noted that there is significant elastic anisotropy between normal and 45° compression, which will be further discussed in Section 4.2.

Post-mortem TEM in Fig. 4(b-c) demonstrates the nature of deformation in both loading orientations. In both loading geometries, deformation occupies a significant fraction of the pillar gage length. The normal compression pillars shear bands at the top of the pillar as seen in Fig. 4(b). However, the shear band does not traverse the width of the pillar, indicating that its propagation is frustrated. Deformation along the gage length of the pillar is indicated by non-zero layer rotation down
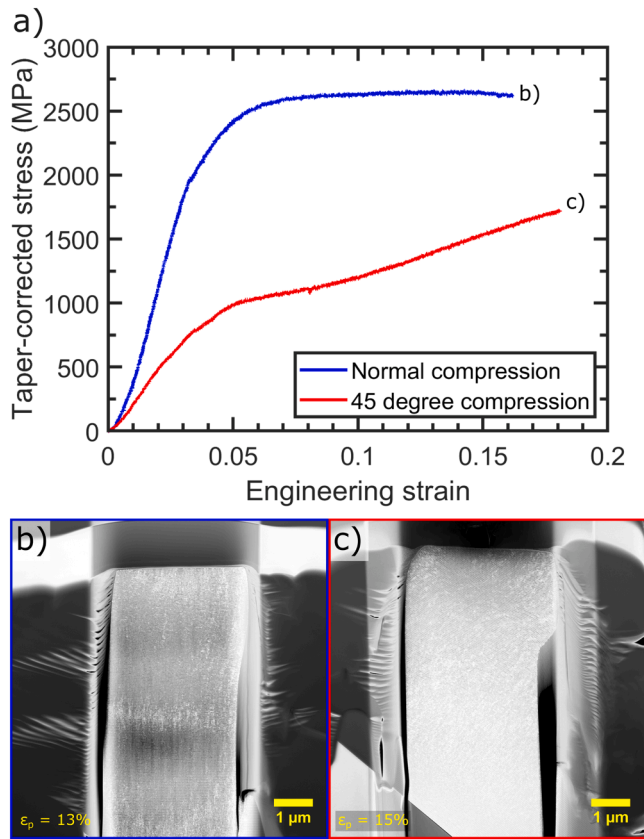
Fig. 4. a) Engineering stress-strain curves for normal and 45° compression pillars. Post-deformation HAADF STEM images of b) layer-normal compression and c) 45° pillars that were sectioned by FIB and imaged using HAADF-STEM.

to the base of the pillar. Fig. 4(c) presents a similar situation for 45° pillars. Material extrusion towards the right side of the pillar occurs in the top third of the deformed pillar, while material below has deformed modestly (also indicated by non-zero layer rotation). The high deformability seen in both loading orientations is atypical for layered nanocrystalline composites, especially at such a fine layer thickness of 10 nm. The delocalized nature of deformation in both loading orientations is likely correlated with the significant work hardening observed. The 45° response is particularly remarkable since this work hardening occurs over a much larger range of plastic strain than in normal compression.

3.2.1. Post-deformation microstructure of layer-normal compression

The deformed 10–10 Cu/Nb microstructure after 0.13 engineering plastic strain under normal compression is analyzed using CTEM and selected area diffraction (SAD) patterns in Fig. 5. Fig. 5(a) depicts the top of the pillar, with an arrested shear band emanating from the top left corner of the pillar. Fig. 5(a) presents regions from which SAD diffraction patterns in Fig. 5(b and c) are taken. Lattice and interface rotation are measured, as these quantities are associated with the shear band formation process in nanolaminates [27,46]. Diffraction patterns near the origin of the shear band show that the grains rotate by an average of about 22°, while inside the shear band the grains rotate by 31°. This lattice rotation is indicative of uneven slip system activation leading to a net shear in the direction of the shear band propagation direction. However, it cannot be trivially correlated to the severity of the shear instability, leading us to turn to other microstructural metrics for shear band analysis.

To quantify the degree of shear localization, the layer normal strain ε_{layer} is characterized as a function of position in Fig. 6. This is defined by:
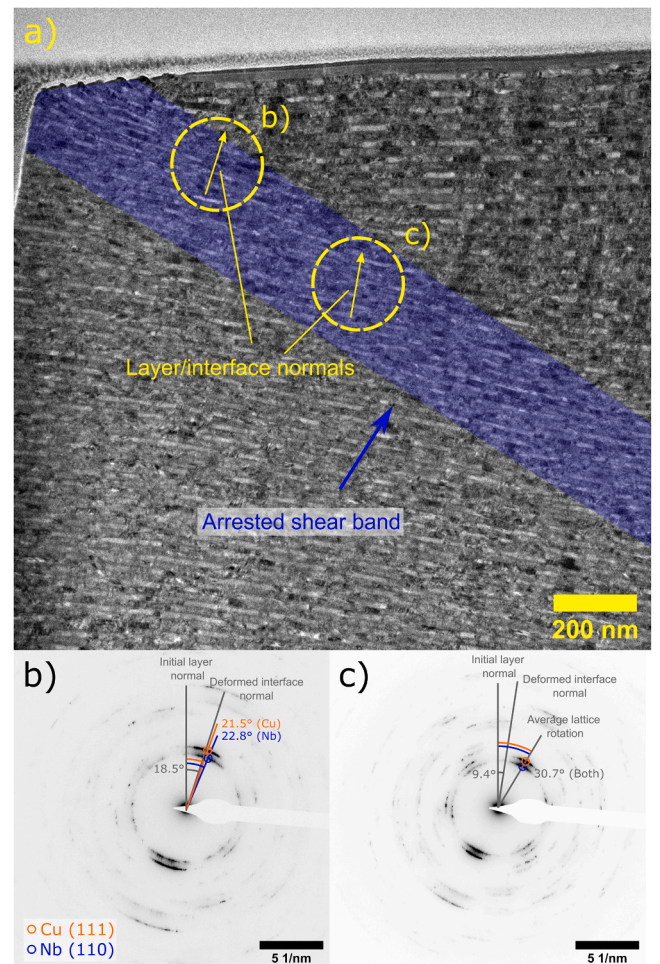
Fig. 5. a) A CTEM micrograph that depicts an arrested shear band that forms in the top of a layer-normal compression pillar in 10–10 Cu/Nb. Note that layer rotation is observed for many layers under the shear band. (b-c) Selected area diffraction (SAD) patterns taken from circles indicated in a). Layer-normal directions are indicated with a yellow arrow in a), which are the same as in (b-c) since CTEM micrographs are aligned with SAD patterns. The maximum extent of lattice rotation is indicated by blue and orange angle markings in (b-c). The centers of diffraction streaks representing compact Cu(111) and Nb(110) planes which were initially oriented parallel to layers are indicated by orange and blue circles in (b-c).

$$\varepsilon_{layer} = \frac{h_o - h_f}{h_o} \tag{1}$$

where h_f is the deformed bilayer thickness measured normal to the rotated interface and h_o is the undeformed bilayer thickness [27,46]. A bilayer includes Cu, Nb, and two 3D interfaces and is used to include interface deformation. ε_{layer} is calculated at the regions indicated in the deformed microstructure depicted in Figure 6(a). h_o is known from Fig. 2 and h_f is found in Fig. 6(a) by measuring the distance across each box in the interface normal direction and dividing by the number of bilayers in the same direction. This gives a bilayer thickness that is measured across several bilayers per box, ensuring a statistically representative ε_{layer} in each box. These strains are plotted as a function of position along the compression axis in Fig. 6(b). ε_{layer} increases rapidly over ~300 nm moving from the material outside of the shear band to the interior of the shear band. The non-shear banded material at the pillar top arises from surface tractions imposed by the flat punch probe and is commonly referred to as "dead metal" in bulk compression tests [58]. Starting from the shear band interior to the regions outside of and below the shear
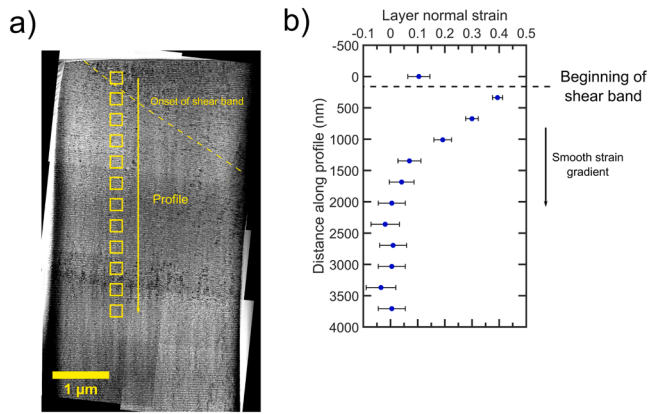
Fig. 6. a) Composite CTEM image depicting a profile along which bilayer thickness measurements were taken. These thicknesses were used to calculate layer normal strain, which are presented in b) as a function of position along the profile. b) is drawn to the scale in a) and aligned such that y-axis values match up with boxes indicated in a). Layer thickness was averaged over each box in a) by dividing the number of layers by the layer-normal distance across the box. Layer normal strain was then calculated with Eq. 1. Error bars are calculated assuming a layer counting error of one layer per box.

band, the ε_{layer} decreases gradually from a peak value of 0.40 to near zero over ~1700 nm. This means that either the bottom of the pillar does not deform or the uncertainty of the ε_{layer} measurements cannot capture deformation in this region. We can resolve this ambiguity by investigating the behavior of the pillar gage length. Fig. S1 demonstrates that the pillar examined in Fig. 6 deforms along the entire gage length. Thus, we can conclude that deformation still occurs far below the shear band in Fig. 6(a). Higher magnification characterization of the shear band in normal compressed 10–10 Cu/Nb can be found in Fig. S3. Fig. S3(a) provides a zoomed in view of the shear band, demonstrating gradual changes in layer normal strain below the onset of the shear band, consistent with the results in Fig. 6. Fig. S3(b) provides chemical mapping of the shear band. This map demonstrates that layer roughening occurs at the most severely strained regions of the shear band. This may indicate that small shear instabilities occurred at very small length scale (~50 nm) [59], but were prevented from coalescing into a fully developed shear band spanning the pillar width.

3.2.2. Post-deformation microstructure after 45° compression

Fig. 7(a) contains cross-sectional CTEM of a 45° compressed Cu/Nb micropillar after 0.15 uniaxial engineering plastic strain. Material is seen bulging out of the side of the pillar in the top 2.5 µm of material, suggesting that some shear localization may have occurred. However, TEM of a pillar deformed to 0.36 total engineering strain presented in Fig. 7(b) demonstrates that this is not the case. The bulged region of the
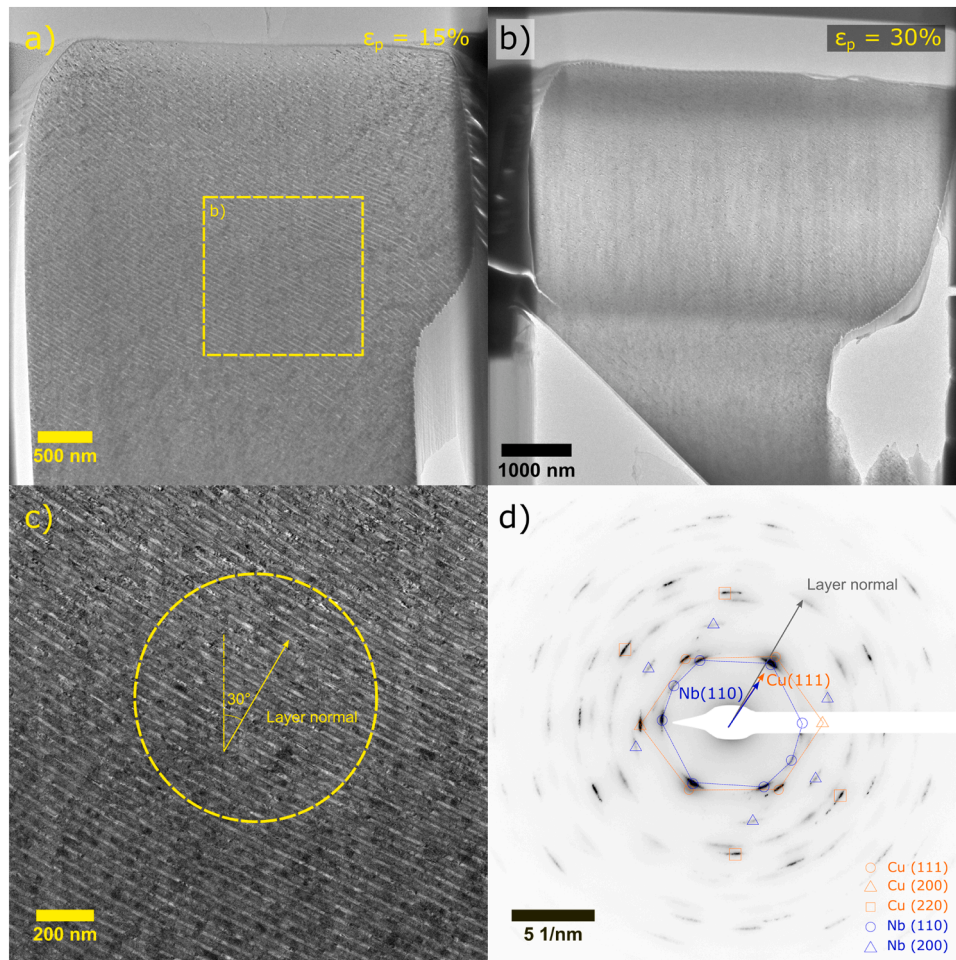
Fig. 7. a) CTEM micrograph of 45° compression sample after 0.15 plastic strain and b) 0.30 plastic strain. c) Higher magnification CTEM micrograph of area of interest in a) denoted by the dotted yellow box. The final orientation of planes parallel to Cu and Nb layers is depicted with respect to the compression axis. d) SAD pattern taken from the area in c) indicated by the dotted yellow circle. Orange and blue arrows depict the orientation of Cu and Nb compact planes that began at 45° incidence to the compression axis, respectively. The grey arrow depicts the orientation of layer/interface planes after compression.

pillar has expanded to encompass the entire gage length, constituting a substantial shape change without abrupt plastic instability. Plastic instability would tend to concentrate strain in the pillar and is generally associated with softening behavior. The stress strain curve for this pillar can be found in Fig. 10, which demonstrates extended work hardening. We also find that Cu/Nb did not rupture at the interfaces in this loading configuration, despite the maximum resolved shear stress aligning with interface planes at the beginning of deformation. This indicates that 3D interfaces can work harden in shear, which is crucial for preventing shear instability.

Microstructural characterization reveals more information on the nature of deformation in 45° compressed 10–10 Cu/Nb. Fig. 7(c) depicts the degree of layer rotation in the region of interest in (a), indicating that layers in this region rotated 15° from their initial orientation. Fig. 7(d) contains a SAD pattern taken from the area depicted in (c), showing that compact planes in Cu and Nb that were parallel to interfaces at the start of deformation rotate the same amount as the interfaces after deformation. This indicates that the Cu, Nb, and 3D interfaces co-deform. This co-deformation provides clues to 3D interface contribution to mechanical behavior, which will be discussed later.

To determine the extent of post-deformation layer thinning, we employ STEM-EDS analysis on the 45° compressed Cu/Nb in Fig. 7(a). Fig. 8(a) and (b) show, respectively, micrographs from the top and bottom of the pillar. Regions indicated in Fig. 8(a-b) were chemically mapped to produce Fig. 8(c-d). Line profiles are drawn in EDS maps to extract chemical profiles, which are then used to calculate the layer and 3D interface thicknesses given in Table 3. The bilayer thicknesses from these measurements suggest little to no layer thinning occurred during deformation. The thinnest bilayer, found from the chemical profile in Fig. 8(c), is 39.4 nm thick, compared to 41.8 nm for undeformed material as determined from Table 3. This reduction in thickness corresponds to a layer-normal strain of 0.06. This amount of strain does not correlate well with the global plastic strain of 0.15, indicating that in this loading orientation layer normal strain is a poor indicator of local strain.

Table 3

Summary of layer thicknesses measured at the top and bottom of 45° compressed Cu/Nb micropillar. h' for 3D interfaces grown on Cu are denoted h'_{3DonCu}, while it is denoted h'_{3DonNb}, for 3D interfaces grown on Nb.

	Pillar top		Pillar bottom	
	Average (nm)	Std. Dev. (nm)	Average (nm)	Std. Dev. (nm)
h_{Cu}	8.9	0.3	10.5	0.6
h_{Nb}	9.5	0.5	10.1	0.3
h'_{3DonCu}	11.1	0.7	11.3	0.6
h'_{3DonNb}	9.7	0.6	10.1	0.4
Bilayer	39.4	0.7	42.2	0.2
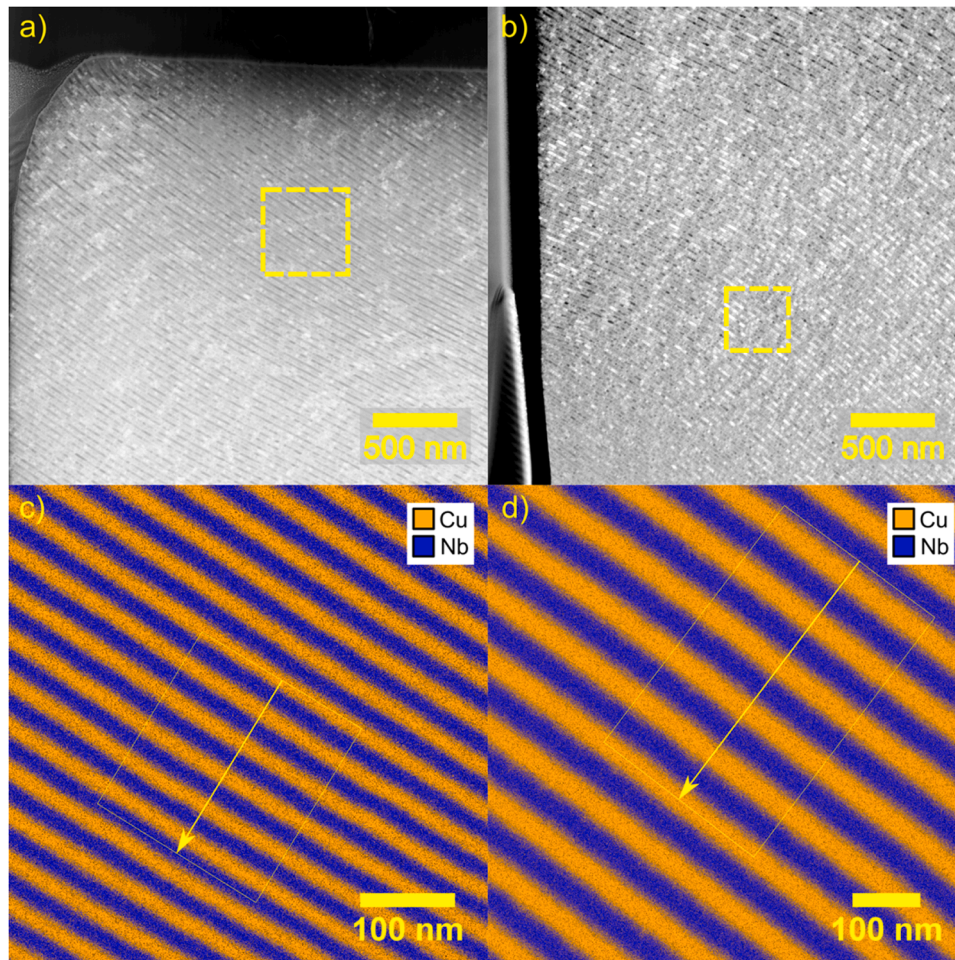
Fig. 8. a) HAADF image of a region near the top of a 45° pillar deformed to 0.18 plastic strain. b) HAADF image of a region near the bottom of a deformed 45° pillar. (c and d) STEM-EDS maps taken from the regions shown in (a-b); c) corresponds to the dotted yellow box in a) and d) corresponds to the dotted yellow box in b). Chemical profiles are taken along the yellow arrows in c) and d) to give layer and interface thicknesses presented in Table 3. Profiles are averaged along the width perpendicular to the arrows depicted by solid yellow boxes in (c-d).

4. Discussion

4.1. Deformation during layer-normal compression

Here, we compare the current work with prior Cu/Nb nanolaminate micropillar compression studies to gain insight into 3D interface mechanical behavior. The previous works focused on 40–10 Cu/Nb with 3D interfaces [46] and 2D interface Cu/Nb with $h = 40$ nm [27]. Fig. 9 compares shear banding between 10–10 3D, 40–10 3D, and $h = 40$ nm 2D Cu/Nb. Here, we quantify shear band intensity by comparing the maximum layer normal strain ε_{layer} normalized by bulk engineering strain ε_{bulk}, as well as maximum strain gradient among different samples. The ε_{bulk} is the absolute value of engineering strain $(l_f - l_o)/l_o$, where l_f and l_o are the post- and pre-deformation micropillar gage lengths. Note that Ref. 27 defines ε_{layer} differently than in Eq. (1), opting for a true strain-like definition. ε_{layer} for this material is recalculated using Eq. (1) for this work. Strain gradients are measured for these materials as follows: ε_{layer} is measured at two locations under the start of the shear band and the difference in ε_{layer} is taken. This difference is divided by the distance Δx between the centers of the regions at which ε_{layer} were measured. Locations are chosen to quantify strain gradient where ε_{layer} changes most rapidly with position. We also investigate if other microstructural metrics associated with shear banding in the literature, *e.g.*, lattice and interface rotation, are good indicators of shear localization intensity. These quantities are summarized in Table 4.

These data show that 10–10 Cu/Nb has the lowest $\varepsilon_{layer}/\varepsilon_{bulk}$, as well as the lowest maximum strain gradient. This is correlated with superior deformability and strength as quantified by previous work [51]. These metrics are also consistent with the delocalized nature of deformation of 10–10 Cu/Nb as demonstrated in Fig. 6. Material with measurable ε_{layer} and interface rotation extends a few microns under the top of the pillar. Additionally, the layer normal strain transitions gradually below the top of the shear band. This contrasts with 40–10 and $h = 40$ nm 2D Cu/Nb, which concentrate strain in a shear band a few hundred nm thick. Thus, we establish quantitatively that 10–10 Cu/Nb deforms in a more delocalized manner compared to the other nanolaminates discussed. We also demonstrate that maximum layer normal strain and maximum strain gradient are good metrics for assessing severity of shear localization. In contrast, the other quantities mentioned here such as lattice and interface rotation do not correlate well with shear localization severity.

Beyond the qualitative relationships established earlier in Ref. 52, quantitative metrics such as maximum layer normal strain and maximum strain gradient can quantify the severity of shear localization in Cu/Nb nanolaminates. Other metrics, such as layer and interface rotation, cannot. We also find that even though strain concentrates in the upper half of the 10–10 Cu/Nb micropillar investigated here, there is evidence of deformation along the entire pillar gage length. To optimize mechanical behavior, we would strive for uniform deformation, which is associated with no strain gradient across the pillar. This has been achieved with interface modification in equiaxed nanocrystalline alloys [60]. Although the highly textured, layered composites studied in this work do not achieve completely uniform deformation, we have demonstrated here that 3D interfaces provide a pathway towards that ideal in anisotropically structured nanocomposites.

The origins of enhanced deformability in 10–10 Cu/Nb lie in the relationship between the geometry of shear banding at the mesoscale and slip system activation at the atomic scale. The gradient in layer-normal strain seen in 10–10 Cu/Nb under layer-normal compression is accompanied by a continuous interface rotation gradient below the shear band. This geometric trend lends support to our hypothesis posed in previous work on 10–10 Cu/Nb [51]. This states that high strength and delocalized deformability in 10–10 Cu/Nb arise from the tendency of 3D interfaces to promote isotropic slip system activation. This change in slip activity compared to 2D interfaces stems from the ability of 3D interfaces to frustrate pileup-assisted slip transfer across heterophase boundaries. This suggests that to achieve completely uniform deformability in nanolaminates, uniform dislocation emission on many slip systems must be encouraged while pileup-assisted slip transfer across multiple layers must be impeded. There may be many ways to achieve this – one way would be to modify the interface structure so that dislocation nucleation sites can be dispersed with high density, uniform distribution, and similar activation stress among all slip systems at 3D interfaces. This is non-trivial and will take careful exploration of the parameter space for 3D interface microstructure in future work.

4.2. Deformation during 45° compression

We can also compare 2D and 3D Cu/Nb in 45° compression using literature results on material with comparable h. Fig. 10(a) shows that $h = 5$ nm 2D Cu/Nb under 45° compression yields at a resolved shear
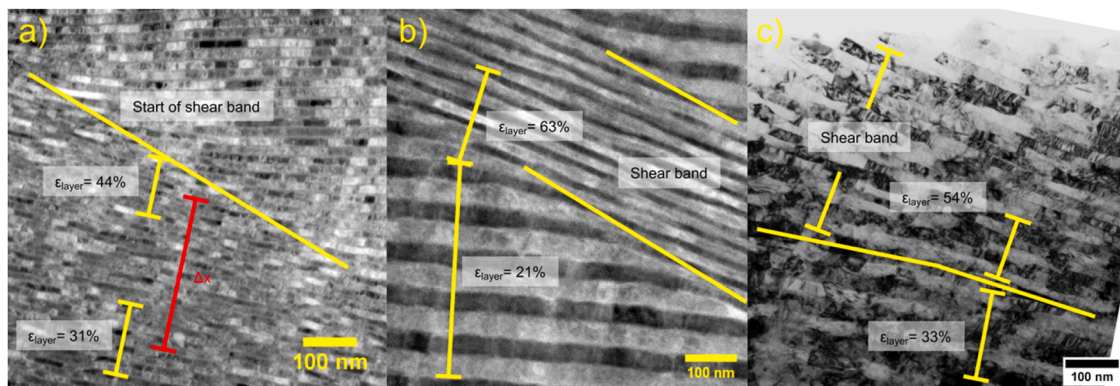

Fig. 9. TEM micrographs of shear bands in a) 10–10 3D interface Cu/Nb, b) 40–10 3D interface Cu/Nb, and c) $h = 40$ nm 2D interface Cu/Nb. (a-b) are HAADF-STEM micrographs, while c) is a bright field CTEM micrograph. c) is adapted from Ref. 27 with permission from AIP Publishing.

Table 4
A summary of shear band microstructural metrics among various Cu/Nb samples. Layer normal strain gradients are presented in percent per nm for readability.

Sample	Bulk strain, ε_{bulk}	Max layer-normal strain, ε_{layer}	$\varepsilon_{layer}/\varepsilon_{bulk}$	ε_{layer} gradient	Lattice rotation	Interface rotation
10–10 3D Cu/Nb	0.16	0.49	3.1	0.045 %/nm	31°	9.4°
40–10 3D Cu/Nb [46]	0.14	0.63	4.5	0.13 %/nm	30°	12°
$h = 40$ nm 2D Cu/Nb [27]	0.14	0.54	5.5	0.12 %/nm	Not measured	17.5°
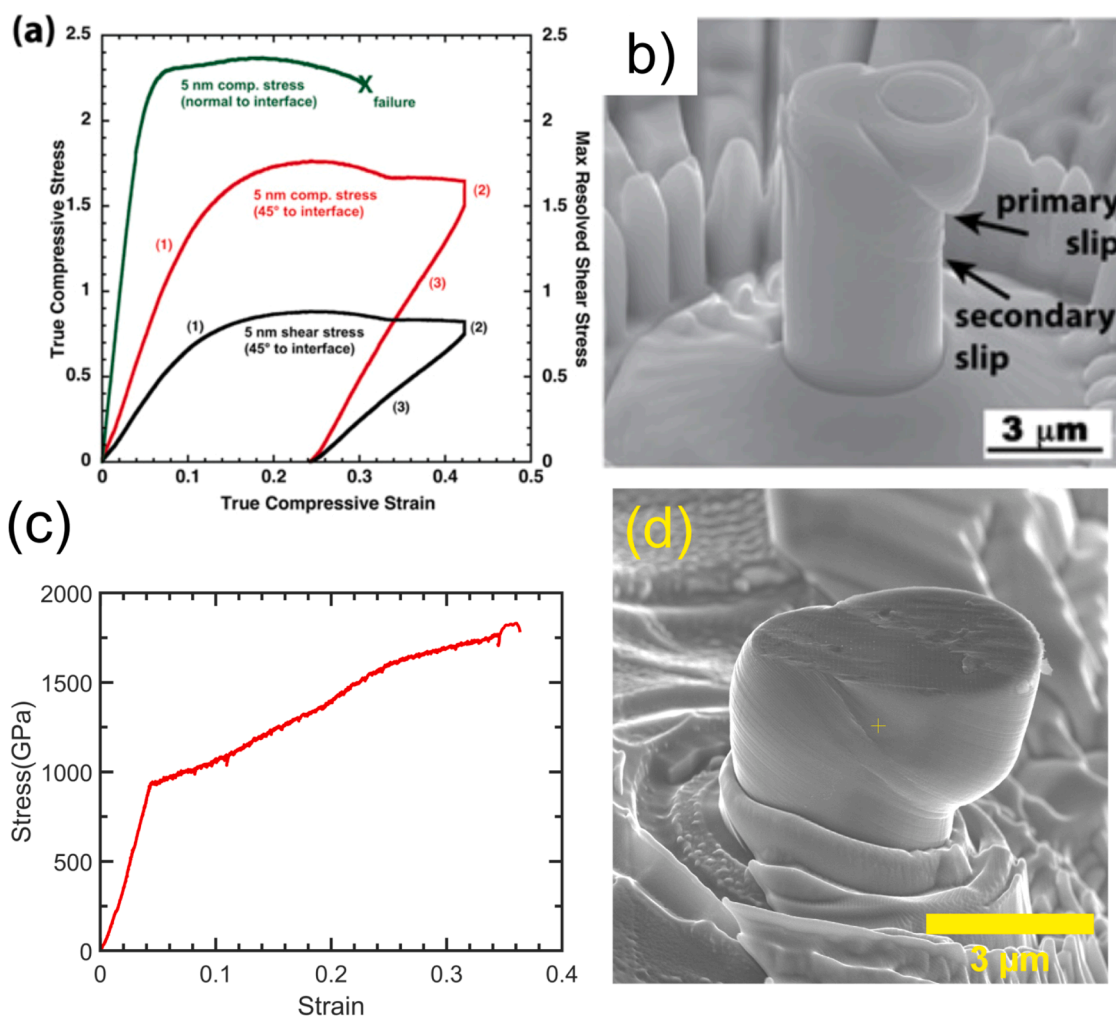
Fig. 10. Comparison of (a-b) h = 5 nm 2D Cu/Nb [61] *ex situ* and (c-d) 10–10 Cu/Nb *in situ* 45° micropillar compression results. From the stress strain curve in a), interfaces in h = 5 nm 2D Cu/Nb yield at about 0.5 GPa true resolved shear stress, and the material work hardens to ultimate compressive stress at 0.25 total true strain (0.15 plastic true strain), then begins strain softening. From the *post mortem* SEM micrograph in b), this material is observed to strain localize heavily at the top of the pillar. In comparison, c) shows that 10–10 Cu/Nb yields at about 0.8 GPa true compressive stress, or 0.4 GPa resolved shear stress. This stress-strain curve shows that 10–10 Cu/Nb does not strain soften like h = 5 nm 2D Cu/Nb. Instead, it work hardens continuously. d) depicts the *post mortem* SEM image of this pillar, which demonstrates the highly delocalized nature of deformation in 10–10 Cu/Nb. (a-b) are reproduced from Ref. 64 with permission from Elsevier.

stress of about 0.5 GPa, and then work hardens to 0.8 GPa shear stress before failure. Failure occurs at 0.15 true plastic strain after subtracting elastic deformation for h = 5 nm 2D Cu/Nb. The pillar undergoes shear localization via sliding along a narrow plane starting near the top of the pillar (Fig. 10(b)) [61]. In contrast, 10–10 Cu/Nb under similar loading yields at a maximum resolved shear stress of 0.4 GPa and then work hardens to a shear stress of 0.9 GPa over an engineering plastic strain of 0.30, as seen in Fig. 10(c). Maximum resolved shear stress is uniaxial normal stress divided by two. Here, 10–10 Cu/Nb deforms over a region a few hundreds of nm wide as seen in Fig. 10(d). This contrasts with its 2D counterpart, where deformation is isolated to a band only a few tens of nanometers wide in Fig. 10(b). This suggests that although yield stress is comparable under 45° pillar compression between 10–10 Cu/Nb and h = 5 nm 2D Cu/Nb, work hardenability and homogeneous deformability are much higher in the 3D interface case. This result demonstrates that composites containing 3D interfaces can work harden appreciably in shear in contrast to 2D interfaces, which undergo significant interfacial sliding and play an important role in shear localization under both normal and 45° pillar compression [27,61].

The shear behavior of 2D Cu-Nb heterophase interfaces can be understood through prior molecular dynamics simulations showing that Kurdjumov-Sachs type Cu-Nb interfaces are relatively weak in shear [62,

63]. Experimentally, 2D Cu-Nb interfaces have been shown to have shear strengths of 0.3–0.55 GPa in h = 5 nm 2D Cu/Nb using *ex situ* 45° micropillar compression (shown in Fig. 10(a and b)) and *in situ* TEM straining experiments [61]. *In situ* results from this work show that after yield, 2D Cu-Nb interfaces slide without work hardening. This explains the highly localized strain observed in the vicinity of the bimetal interface. Comparing the shear strength of 2D interfaces to that of the abutting phases, we see that the critical resolved shear stresses of pure Cu and Nb below a grain size of 100 nm are at least 0.43 and 1.0 GPa, respectively (assuming a Schmid factor of 0.5) [64]. Thus, the limiting strength in this material is in either Cu or the interfaces. After yield in either of these regions, little work hardening occurs.

While we do not have any direct evidence for the shear strength of 3D interfaces, we can place its lower bound at 0.4 GPa from the micropillar data in Fig. 10(c). This is close to the critical resolved shear stress of pure nanocrystalline Cu. Therefore, it is likely that during the early stages of plastic deformation in 3D Cu/Nb, Cu layers and 3D interfaces work harden together to produce the delocalized deformation seen in Fig. 10 (d). Once they harden to match the high Nb flow stress, the entire composite can continue work hardening at the same rate. We also find that 3D interfaces enhance work hardenability in the nominally soft Cu phase. Pure nanocrystalline copper (nc Cu) with a grain size of 100 nm

can work harden from a yield stress of 0.5 GPa to 0.8 GPa under uniaxial compression [65]. This grain size is used because it is the in-plane grain size of Cu grains in 10–10 Cu/Nb (see Fig. S4). Here, we see that the Cu phase in 3D Cu/Nb can work harden to possess a maximum resolved shear stress more than 1.0 GPa. In other words, without the constraints imposed by 3D interfaces, Cu and Nb layers would have divergent flow stresses. Evidence of this divergent plastic behavior is found in TEM of 45° compressed 10–10 Cu/Nb in Fig. S5, where material extruded out to the pillar surface assumes a serrated morphology. Once Cu and Nb are extruded out to a free surface, they flow differently in the absence of 3D interfaces.

As an aside, Fig. 10(a) shows that there is apparently significant elastic anisotropy between normal and 45° compression for $h = 5$ nm 2D Cu/Nb, just like there is for 10–10 Cu/Nb in Fig. 4. Some of this may originate from differences in substrate compliance. The loading stiffness of micropillars can be affected by substrate morphology due to the pillar acting as a rigid flat punch [66]. However, a significant portion of the difference in elastic loading stiffness between normal and 45° compression in Cu/Nb can be attributed to real differences in elastic constants. The elastic constants of Cu and Nb are presented in Table 5, giving Zener ratios of 3.20 and 0.574 for Cu and Nb, respectively [67]. Elastically isotropic materials have Zener ratios of 1, so Cu and Nb are significantly elastically anisotropic. This leads to the elastic anisotropy between normal and 45° compression in $h = 5$ nm 2D Cu/Nb and 10–10 Cu/Nb.

The results shown above for 45° compression have demonstrated two remarkable aspects of the influence of 3D interfaces on plastic deformation under shear loading. The first is that 3D interfaces have at least comparable interfacial shear strength, but much superior work hardenability compared to their 2D counterparts. The second is that 3D interfaces mediate codeformation and superior work hardenability in abutting pure layers. These behaviors can be explained by examining the distribution of slip on different slip systems in Cu and Nb.

4.2.1. Schmid analysis of 45° compression

The delocalized deformation and work hardening observed in 45° 10–10 Cu/Nb is somewhat surprising given the anisotropic nature of the material. One might expect that slip should favor either interfaces or only the Cu {111}<110> and Nb {110}<111> slip systems oriented parallel to the interface and layer planes, since these features are aligned along the direction of maximum resolved shear stress. To elucidate the expected slip pathways in 10–10 Cu/Nb, we investigate the role of Schmid factors on slip system activation. Using the texture measurement in Fig. 3, the Schmid factor is calculated for slip systems that are oriented for 45° compression for a range of rotation angles about the interface normal direction. Fig. 11 shows that slip on planes parallel to layers is geometrically favored for most crystal orientations in the fiber texture, but some orientations favor slip on non-layer parallel systems. In addition, many orientations in which a layer parallel slip system has the highest Schmid factor also contain non-layer parallel slip systems that are close in Schmid factor to the most favored system. Assuming different slip systems work harden independently, modest work hardening on layer-parallel slip systems can trigger slip on non-layer parallel slip systems. Only small amounts of lattice rotation are needed to re-orient the material to favor layer non-parallel slip systems. Since we have shown in Fig. 7 that deformation induces lattice rotation in 10–10 Cu/Nb, the distribution of slip on different slip systems needs to be known as a function of strain. We quantify this using CPFE simulations.
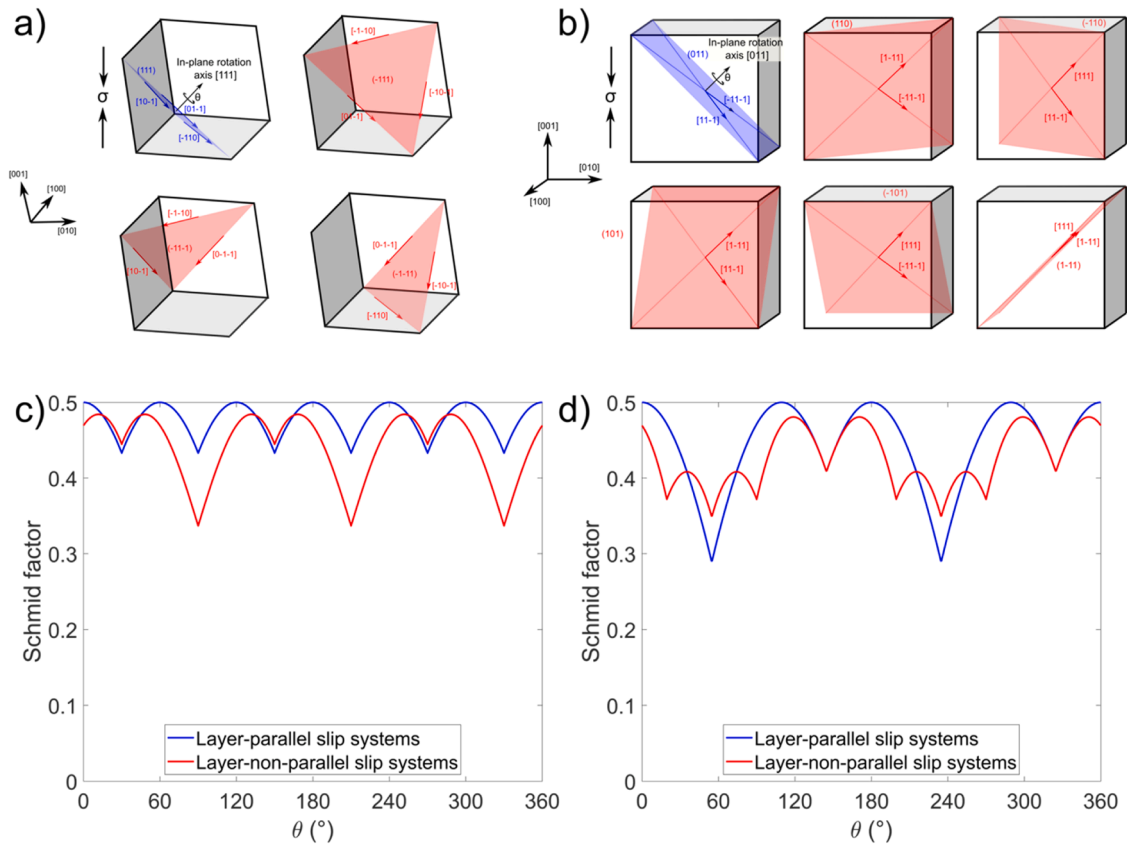
4.2.2. CPFE modeling of 45° compression

Crystal Plasticity Finite Element (CPFE) is used to evaluate slip system activity in 45° compressed 10–10 Cu/Nb [53]. We use the same 3D finite element 45° laminate model constructed in prior work [68], which is composed of linear tetrahedral C3D4 elements. The model microstructure consists of alternating Cu and Nb nanocrystalline layers. Each layer is spanned by one grain in the interface normal direction. The orientations of the grains are assigned according to the measured texture in Fig. 3 and the orientation relationship of Cu/Nb grain pairs across the interface is chosen to be Kurdjumov-Sachs. The elastic anisotropy of Cu and Nb phases is accounted for in this model. The three independent elastic constants of the stiffness tensor C are taken from experimental measurements and given in Table 5 [69]. Plastic strain is accommodated by crystallographic slip on the {111}<110> slip systems for Cu and the {110}<111> slip systems for Nb. For simplicity, the slip strength used to activate each slip system in the flow rule in the CPFE constitutive law is assumed constant and equal among the slip systems within each phase. These are the only two unknowns in the hardening law and are estimated from fits to the yield strength measured experimentally. They are estimated to be 80 MPa in Cu and 485 MPa in Nb. These values are reasonable for two reasons. First, it is expected that the dislocations in Nb would be harder to move than in Cu and that both values would be higher than the slip strengths for the same dislocations in their coarse-grained form. Second, these values represent a nominal resistance from other defects in the nanostructure and not solely lattice friction. It should be noted that the Cu CRSS is relatively low for a nanocrystal, and reflects the ease of forming dislocations from the GBs in the Cu layers between the interfaces [69]. These nucleation sites can be activated due to the loading orientation of 45° compression. In other orientations such as normal compression, dislocation nucleation must occur at Cu-Nb interface/GB intersections [70], which can require stresses that are an order of magnitude larger than stresses required for pure GB nucleation. Since the goal of these calculations was to gain basic insight on slip patterns in the 45° test, no attempt was made to explicitly account for multiple obstacles, such as interfaces, grain boundaries, other dislocations, and defects. It is important to note that this approach models 3D interfaces better than 2D interfaces; as discussed in Section 4.2, 2D interfaces are either weaker or less work hardenable than 3D interfaces. To tailor the CPFE model to 2D interfaces well, weak traction at heterophase interfaces would have to be included. Since this model ensures compatible deformation, it approximates strong interfacial traction associated with 3D interfaces well. The model has periodic boundary conditions in all three spatial dimensions. In the deformation simulations, the deformation of each pair of boundary faces is equal and the stress tensors opposite in sign. Compression is only applied normal to the top face so that like in the experiment, the loading is 45° to the Cu/Nb interface planes. The deformation is applied in fine strain increments and at each increment the total stress and slip activity in each grain in each layer are determined.

CPFE results are presented in Fig. 12. The flow rules used for Cu and Nb were able to fit experimental behavior well as seen in Fig. 12(b). The evolution of layer parallel and non-layer parallel slip is presented as a function of strain in Fig. 12(c-d). For both Cu and Nb phases, most slip occurs on non-layer-parallel slip systems at yield. As deformation progresses, the distribution of slip does not change significantly. It is important to note that if slip were evenly distributed over all slip systems, then 25% of slip would occur on layer-parallel systems in Cu (3 layer-parallel and 9 non-layer-parallel slip systems) and 16.6% of slip would occur on layer-parallel systems in Nb (2 layer-parallel and 10 non-layer-parallel slip systems). Since layer-parallel slip only accounts for ~11% of activated slip in both phases, layer-parallel slip systems are under-represented during deformation. This runs counter to the Schmid factor calculations in Fig. 11, signifying that other factors such as flow stress mismatch and traction at heterophase interfaces and grain boundaries, taken into account in the CPFE simulation, have an outsized effect on the distribution of slip on different slip systems in Cu and Nb. In

Table 5
Elastic constants of single crystal Cu and Nb used in the CPFE simulation.

Phase	C_{11}(GPa)	C_{12}(GPa)	C_{44}(GPa)
Cu	168.4	121.4	75.4
Nb	234	134	28.7

Fig. 11. Depictions of slip systems in a) Cu and b) Nb. In Cu, 1 slip plane containing 3 slip directions is parallel to the direction of maximum resolved shear stress and is layer-parallel. 3 slip planes with 3 slip directions each are non-layer parallel. In Nb, 1 slip plane containing 2 slip directions is layer-parallel, while 5 slip planes containing 2 slip directions each are non-layer parallel. The maximum Schmid factor found in layer-parallel and non-layer parallel slip systems are plotted for c) Cu and d) Nb as a function of in-plane rotation.

addition, the CPFE results show that most slip in 45° compressed 10–10 Cu/Nb occurs on slip systems that intersect the 3D interfaces over the entire range of strain investigated. This means that 3D interface-dislocation interactions must cause extended deformability without plastic instability observed in 45° compression, which will be discussed next.

4.3. Mechanism of enhanced plasticity in 10–10 Cu/Nb

4.3.1. Influence of 3D interface on dislocation activity

Here, we propose a mechanism of 3D interface-enabled plasticity. Previous work has shown that when h is on the order of a few 10 s of nm, a deformation mechanism called confined layer slip (CLS) plausibly dominates nanolaminate material strength [26,52]. A schematic of this deformation mode is found in Fig. 13(a). Here, a dislocation hairpin loop is propagating along a non-interface parallel slip system. The propagation direction is chosen to be parallel to the layer. This is because the in-plane grain size of 10–10 Cu/Nb is much larger than the layer thickness, as seen in Fig. S4. We assume that the material cannot sustain a hairpin loop or multiple dislocations along slip directions at acute angles to the interface. The loop with slip direction parallel to the layer is under applied shear stress τ, with a Burgers vector oriented such that screw segments lie parallel to 3D interfaces and a mixed segment of semicircular geometry leads the hairpin. Under the applied stress, Peach-Koehler forces $\underline{F}_1$, $\underline{F}_2$, and $\underline{F}_3$ are exerted on the hairpin loop at the indicated locations in Fig. 13(a). We propose that in 10–10 3D Cu/Nb under both normal and 45° compression, plasticity without plastic instability occurs because of dislocation-interface interactions depicted in Fig. 13(b). If a second dislocation is nucleated on the same slip system

as the loop in Fig. 13(a), then it will form a second hairpin loop with smaller radius than the first. This is because of the presence of 3D interfaces. For 3D Cu/Nb shown in Fig. 13(a and b), the screw segments are blocked from absorption into or transmission across the 3D interfaces. This is supported by previous PFDD simulations demonstrating that 3D interfaces resist slip transfer caused by single dislocations or dislocation pileups [51]. This contrasts with 2D Cu/Nb, where previous work containing direct observation of CLS demonstrates that these segments likely deposit in the 2D interface, leaving a residual Burgers vector in the interface structure (Fig. 13(c)) [52]. These experiments are supported by molecular dynamics work that shows that it is energetically favorable for 2D PVD Cu/Nb interfaces to absorb incoming glide dislocations [39,42]. A subsequent dislocation on the same slip system in 2D Cu/Nb would have the same hairpin radius, and thus the same stress barrier to motion as the first loop. This follows from equations derived for Orowan bowing that give a $\frac{\ln(h)}{h}$ dependence of the critical stress required to move the dislocation. Thus, the force required to move the leading portion of the second loop would be the same as in the first, $\underline{F}_2$. Now, we can turn our attention to the second hairpin loop in 3D Cu/Nb as shown in Fig. 13(b). Due to repulsive interactions between dislocations with the same Burgers vector, the second loop has a smaller leading radius than the first. Alternatively, the second loop has a lower effective h than the first loop. Thus, the second loop requires greater stress, or equivalently greater force $\underline{F}_4$, to move than the first loop. We quantify this in the Supplementary Information for normal compression, where results from Fig. S6 and Table S1 show that the second loop requires 19.0 GPa to move in Cu, while in Nb it requires 3.85 GPa. Both values are much higher than the observed flow stress of the material. In addition, the second loop would introduce unrealistically high strain
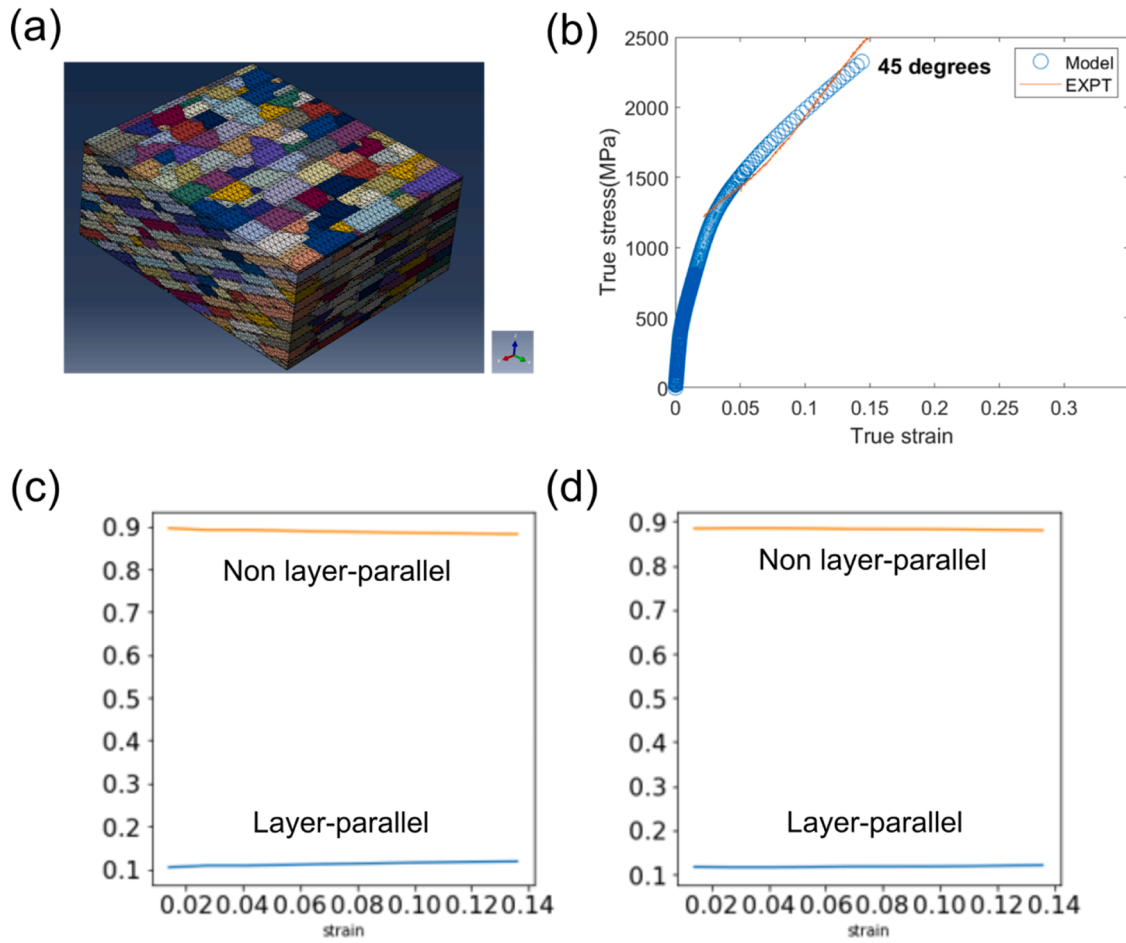
Fig. 12. a) Setup of simulation box used for CPFE. Grains are oriented so that one set of compact Cu (111) and Nb (110) planes is oriented 45° to the compression axis. b) A comparison of the experimental plastic stress-strain curve from Fig. 4 and the stress strain curve produced by the CPFE simulation. Slip evolution is presented for c) Cu and d) Nb, where slip systems are grouped according to parallel and non-parallel slip plane alignment to Cu-Nb heterophase interfaces.
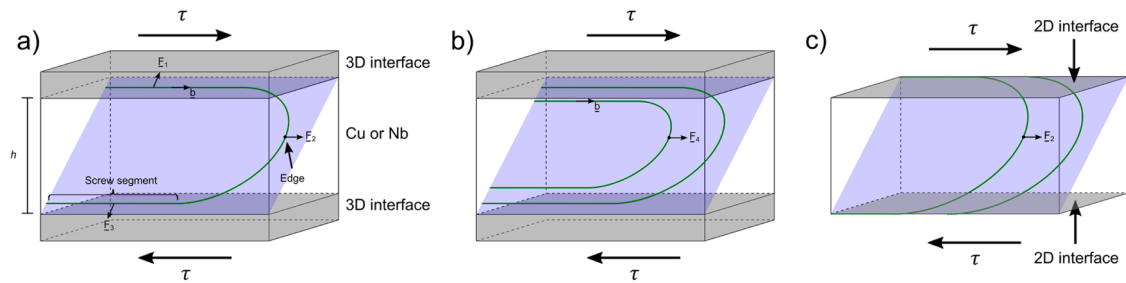
Fig. 13. a) A single hairpin loop in a pure layer in 3D Cu/Nb. The active slip plane is depicted in blue, the 3D interfaces are shaded in gray, and the loop is represented by a green line. The Burgers vector is also shown, allowing for identification of screw and mixed segments of the dislocation line. Forces on these segments are shown by $\underline{F}_1$, $\underline{F}_2$, and $\underline{F}_3$. If another dislocation loop is nucleated on the same slip system as in a), the dislocation arrangement in b) arises. Here, the second dislocation line must have force $\underline{F}_4$ exerted on it for it to propagate. Since it has lesser radius than the first loop, $\underline{F}_4$ must be higher in magnitude than $\underline{F}_2$, making it unfavorable to propagate. This contrasts with 2D Cu/Nb shown in c), where deposition of edge segments in the interface means that the second hairpin loop has the same radius as the first, and thus the same critical stress for propagation.

energy. This is because the stress field of the second loop's trailing screw segments would repel each other strongly due to the small radius of the leading segment of the loop (also addressed in the Supplementary Information). Because of the multiple factors making propagation of the second loop energetically unfavorable, deformation must occur by some other mechanism. We propose that slip must activate in a grain elsewhere in the material, or in the same grain on a slip system with non-maximal Schmid factor. In either case, dislocation storage is enhanced in the pure layers and uniform deformability is enabled.

4.3.2. Role of 3D interface shear strength

Insights on 3D interface shear strength from 45° compression add to the understanding of mechanical behavior in layer-normal compression. It is known that in 2D Cu/Nb, interface sliding caused by low 2D interface shear strength induces shear localization under layer-normal compression [27]. 45° compression tests in this work show that not only are 3D interfaces strong in shear, but they are also work hardenable. Therefore, 3D interfaces prevent interface sliding and allow 10–10 Cu/Nb to deform homogeneously to large strain and work harden

significantly in normal compression. These observations at the micropillar length scale can be rationalized by literature results on the atomic-scale mechanical behavior of 2D interfaces. It is known that the low interfacial shear strength of PVD 2D Cu/Nb interfaces allows incoming glide dislocation cores to enter the interface, spread, and become trapped in the interface [62]. This means that 2D interfaces can act as effective dislocation traps [71,72] and can strengthen materials under certain loading conditions [26]. However, they come with the price of early shear localization in other loading conditions like uniaxial compression [27]. Following this train of logic, we might expect the high strength and work hardenability of 3D interfaces to inhibit glide dislocation core absorption. It has already been shown that 3D interfaces hinder the transit of dislocations between abutting crystals using PFDD [49–51]. While PFDD incorporates atomic scale information of constituent phases such as crystal structure, lattice parameter, generalized stacking fault energy curve, etc., it does not explicitly model atomic scale structure of interfaces as has been done using molecular dynamics for 2D interfaces [39,73]. Further atomistic work should be done to study the interplay between 3D interface shear strength and its influence on the movement and activity of dislocations on the atomic scale. This work demonstrates that understanding of interface shear behavior using 45° compression tests can be used to explain mechanical behavior observed in other loading configurations in 2D and 3D Cu/Nb. Thus, interfacial shear strength should play a principal role in the search for ever stronger and deformable nanostructured alloys.

5. Conclusions

This work has quantified differences in mechanical behavior and the tendency to undergo shear instability between 2D and 3D Cu/Nb composites in two different loading conditions. Under layer-normal compression, we show that out of 10–10 Cu/Nb, 40–10 Cu/Nb, and h = 40 nm 2D Cu/Nb, shear localization is the least severe in 10–10 Cu/Nb. Qualitatively, this is apparent from the highly delocalized nature of deformation in 10–10 Cu/Nb. Quantitatively, 10–10 Cu/Nb has the lowest maximum layer-normal strain and a layer-normal strain gradient that is almost three times lower than found in 40–10 Cu/Nb and h = 40 nm 2D Cu/Nb. Smooth gradients in layer-normal strain and layer rotation in 10–10 Cu/Nb are indicative of isotropic slip system activation due to discouraged interlayer slip transfer in Cu/Nb with high 3D interface content. Under 45° compression, we show that 3D Cu/Nb work hardens 100 MPa more than 2D Cu/Nb at similar h values in terms of resolved shear stress. Deformability is also improved for 10–10 Cu/Nb in 45° compression, which can undergo 0.15 more strain than 2D Cu/Nb without plastic instability. Slip evolution provided by CPFE simulation shows layer-parallel slip events are underrepresented by 14% in Cu and 5.6% in Nb as compared to isotropic slip system activation. This shows that most slip intersects 3D interfaces during plastic deformation, further suggesting that 3D interfaces possess high strength. The simulation work allowed us to present a mechanism of enhanced plasticity in 45° compression involving dislocation hairpin loop-3D interface interactions. We quantifiably show that 10–10 Cu/Nb prefers single-dislocation propagation on different slip systems or in spatially separated locations, leading to enhanced deformability and work hardening. These experiments also show that interfacial shear strength and work hardenability are a key metrics to optimize in the creation of strong and deformable nanocomposites and nanostructured alloys. Overall, 3D interfaces enhance mechanical properties seen in both layer normal and 45° compression. 3D Cu/Nb is highly deformable in both loading conditions, demonstrating that manipulation of interface structure can optimize mechanical behavior of nanocrystalline alloys under multiple stress states.

Declaration of competing interest

The authors declare that they have no known competing financial interests or personal relationships that could have appeared to influence the work reported in this paper.

Supplementary materials

Supplementary material associated with this article can be found, in the online version, at doi:10.1016/j.actamat.2024.119697.

References

[1] M.A. Meyers, A. Mishra, D.J. Benson, Mechanical properties of nanocrystalline materials, Prog. Mater. Sci. 51 (2006) 427–556.

[2] C.C. Koch, D.G. Morris, K. Lu, A. Inoue, Ductility of nanostructured materials, MRS Bull 24 (1999) 54–58.

[3] Y.T. Zhu, X. Liao, Retaining ductility, Nat. Mater. 3 (2004) 351–352.

[4] C.C. Koch, Optimization of strength and ductility in nanocrystalline and ultrafine grained metals, Scr. Mater. 49 (2003) 657–662.

[5] E. Ma, Eight routes to improve the tensile ductility of bulk nanostructured metals and alloys, JOM 58 (2006) 49–53.

[6] A. Khalajhedayati, Z. Pan, T.J. Rupert, Manipulating the interfacial structure of nanomaterials to achieve a unique combination of strength and ductility, Nat. Commun. 7 (2016) 10802.

[7] S.C. Pun, W. Wang, A. Khalajhedayati, J.D. Schuler, J.R. Trelewicz, T.J. Rupert, Nanocrystalline Al-Mg with extreme strength due to grain boundary doping, Mater. Sci. Eng. A 696 (2017) 400–406.

[8] E. Ma, Y.M. Wang, Q.H. Lu, M.L. Sui, L. Lu, K. Lu, Strain hardening and large tensile elongation in ultrahigh-strength nano-twinned copper, Appl. Phys. Lett. 85 (2004) 4932–4934.

[9] Q. Li, S. Xue, J. Wang, S. Shao, A.H. Kwong, A. Giwa, Z. Fan, Y. Liu, Z. Qi, J. Ding, H. Wang, J.R. Greer, H. Wang, X. Zhang, High-strength nanotwinned Al alloys with 9R phase, Adv. Mater. 30 (2018) 1704629.

[10] H. Oka, M. Watanabe, N. Hashimoto, S. Ohnuki, S. Yamashita, S. Ohtsuka, Morphology of oxide particles in ODS austenitic stainless steel, J. Nucl. Mater. 442 (2013) S164–S168.

[11] J.G. Kim, N.A. Enikeev, J.B. Seol, M.M. Abramova, M.V. Karavaeva, R.Z. Valiev, C. G. Park, H.S. Kim, Superior strength and multiple strengthening mechanisms in nanocrystalline TWIP steel, Sci. Rep. 8 (2018) 1–10.

[12] H. Van Swygenhoven, J.R. Weertman, Deformation in nanocrystalline metals, Mater. Today 9 (2006) 24–31.

[13] I.J. Beyerlein, M.J. Demkowicz, A. Misra, B.P. Uberuaga, Defect-interface interactions, Prog. Mater. Sci. 74 (2015) 125–210.

[14] L. Lu, X. Chen, X. Huang, K. Lu, Revealing the maximum strength in nanotwinned copper, Science 323 (2009) 607–610 (1979).

[15] Y.F. Shen, L. Lu, M. Dao, S. Suresh, Strain rate sensitivity of Cu with nanoscale twins, Scr. Mater. 55 (2006) 319–322.

[16] J. Wang, X. Zhang, Twinning effects on strength and plasticity of metallic materials, MRS Bull 41 (2016) 274–281.

[17] J.P. Liebig, S. Krauß, M. Göken, B. Merle, Influence of stacking fault energy and dislocation character on slip transfer at coherent twin boundaries studied by micropillar compression, Acta Mater. 154 (2018) 261–272.

[18] P.M. Anderson, T. Foecke, P.M. Hazzledine, Dislocation-based deformation mechanisms in metallic nanolaminates, MRS Bull 24 (1999) 27–33.

[19] A. Misra, H. Kung, Deformation behavior of nanostructured metallic multilayers, Adv. Eng. Mater. 3 (2001) 217–222.

[20] A. Sáenz-Trevizo, A.M. Hodge, Nanomaterials by design: a review of nanoscale metallic multilayers, Nanotechnology 31 (2020) 292002.

[21] Y.F. Zhao, J.Y. Zhang, Y.Q. Wang, K. Wu, G. Liu, J. Sun, Unusual plastic deformation behavior of nanotwinned Cu/high entropy alloy FeCoCrNi nanolaminates, Nanoscale 11 (2019) 11340–11350.

[22] J.Y. Zhang, Y. Liu, J. Chen, Y. Chen, G. Liu, X. Zhang, J. Sun, Mechanical properties of crystalline Cu /Zr and crystal – amorphous Cu / Cu – Zr multilayers, Mater. Sci. Eng. A 552 (2012) 392–398.

[23] M. Jain, K. Yaddanapudi, A.T. Kidigannappa, K. Baldwin, M. Knezevic, N.A. Mara, I.J. Beyerlein, S. Pathak, Simultaneous high strength and mechanical stability of bcc Nb/Mg nanolaminates, Acta Mater. 242 (2023) 118487.

[24] S. Jiang, L. Bai, Q. An, Z. Yan, W. Li, K. Ming, S. Zheng, Dependence of plastic stability on 3D interface layer in nanolaminated materials, Acta Metall. Sin. 35 (2022) 1759–1764.

[25] I.J. Beyerlein, N.A. Mara, J. Wang, J.S. Carpenter, S.J. Zheng, W.Z. Han, R. F. Zhang, K. Kang, T. Nizolek, T.M. Pollock, Structure–property–functionality of bimetal interfaces, JOM 64 (2012) 1192–1207.

[26] A. Misra, J.P. Hirth, R.G. Hoagland, Length-scale-dependent deformation mechanisms in incoherent metallic multilayered composites, Acta Mater. 53 (2005) 4817–4824.

[27] N.A. Mara, D. Bhattacharyya, J.P. Hirth, P. Dickerson, A. Misra, Mechanism for shear banding in nanolayered composites, Appl. Phys. Lett. 97 (2010) 021909.

[28] W.Z. Han, J.S. Carpenter, J. Wang, I.J. Beyerlein, N.A. Mara, Atomic-level study of twin nucleation from face-centered-cubic/body- centered-cubic interfaces in nanolamellar composites, Appl. Phys. Lett. (2012) 100.

[29] W.Z. Han, E.K. Cerreta, N.A. Mara, I.J. Beyerlein, J.S. Carpenter, S.J. Zheng, C. P. Trujillo, P.O. Dickerson, A. Misra, Deformation and failure of shocked bulk Cu-Nb nanolaminates, Acta Mater. 63 (2014) 150–161.

[30] R.G. Hoagland, R.J. Kurtz, The relation between grain-boundary structure and sliding resistance, Philos. Mag. A 82 (2002) 1073–1092.

[31] S. Dong, T. Chen, S. Huang, N. Li, C. Zhou, Thickness-dependent shear localization in Cu/Nb metallic nanolayered composites, Scr. Mater. 187 (2020) 323–328.

[32] T. Ajantiwalay, X. Ma, A. Yu, M. Pole, J. Silverstein, S. Mathaudhu, A. Devaraj, B. Gwalani, Shear deformation of pure-Cu and Cu/Nb nano-laminates using micromechanical testing, Scr. Mater. 230 (2022) 115402.

[33] C. Ding, J. Xu, X. Li, D. Shan, B. Guo, T.G. Langdon, Microstructural evolution and mechanical behavior of Cu/Nb multilayer composites processed by accumulative roll bonding, Adv. Eng. Mater. 22 (2020) 1–12.

[34] K. Yu-Zhang, J.D. Embury, K. Han, A. Misra, Transmission electron microscopy investigation of the atomic structure of interfaces in nanoscale Cu-Nb multilayers, Philos. Mag. 88 (2008) 2559–2567.

[35] S.-B. Lee, J.E. LeDonne, S.C.V. Lim, I.J. Beyerlein, A.D. Rollett, The heterophase interface character distribution of physical vapor-deposited and accumulative roll-bonded Cu–Nb multilayer composites, Acta Mater. 60 (2012) 1747–1761.

[36] I.J. Beyerlein, N.A. Mara, J.S. Carpenter, T. Nizolek, W.M. Mook, T.A. Wynn, R. J. McCabe, J.R. Mayeur, K. Kang, S. Zheng, J. Wang, T.M. Pollock, Interface-driven microstructure development and ultra high strength of bulk nanostructured Cu-Nb multilayers fabricated by severe plastic deformation, J. Mater. Res. 28 (2013) 1799–1812.

[37] R.F. Zhang, I.J. Beyerlein, S.J. Zheng, S.H. Zhang, A. Stukowski, T.C. Germann, Manipulating dislocation nucleation and shear resistance of bimetal interfaces by atomic steps, Acta Mater. 113 (2016) 194–205.

[38] X.F. Kong, I.J. Beyerlein, Z.R. Liu, B.N. Yao, D. Legut, T.C. Germann, R.F. Zhang, Stronger and more failure-resistant with three-dimensional serrated bimetal interfaces, Acta Mater. 166 (2019) 231–245.

[39] W.R. Jian, Y. Su, S. Xu, W. Ji, I.J. Beyerlein, Effect of interface structure on dislocation glide behavior in nanolaminates, J. Mater. Res. 36 (2021) 2802–2815.

[40] N.A. Mara, I.J. Beyerlein, Review: effect of bimetal interface structure on the mechanical behavior of Cu-Nb fcc-bcc nanolayered composites, J. Mater. Sci. 49 (2014) 6497–6516.

[41] M.J. Demkowicz, L. Thilly, Structure, shear resistance and interaction with point defects of interfaces in Cu-Nb nanocomposites synthesized by severe plastic deformation, Acta Mater. 59 (2011) 7744–7756.

[42] J. Wang, R.G. Hoagland, J.P. Hirth, A. Misra, Atomistic simulations of the shear strength and sliding mechanisms of copper-niobium interfaces, Acta Mater. 56 (2008) 3109–3119.

[43] A. Misra, J.P. Hirth, R.G. Hoagland, J.D. Embury, H. Kung, Dislocation mechanisms and symmetric slip in rolled nano-scale metallic multilayers, Acta Mater. 52 (2004) 2387–2394.

[44] N.A. Mara, D. Bhattacharyya, P. Dickerson, R.G. Hoagland, A. Misra, Deformability of ultrahigh strength 5nm Cu/Nb nanolayered composites, Appl. Phys. Lett. 92 (2008) 231901.

[45] S.J. Zheng, J. Wang, J.S. Carpenter, W.M. Mook, P.O. Dickerson, N.A. Mara, I. J. Beyerlein, Plastic instability mechanisms in bimetallic nanolayered composites, Acta Mater. 79 (2014) 282–291.

[46] Y. Chen, N. Li, R.G. Hoagland, X.Y. Liu, J.K. Baldwin, I.J. Beyerlein, J.Y. Cheng, N. A. Mara, Effects of three-dimensional Cu/Nb interfaces on strengthening and shear banding in nanoscale metallic multilayers, Acta Mater. 199 (2020) 593–601.

[47] S. Xu, J.Y. Cheng, Z. Li, N.A. Mara, I.J. Beyerlein, Phase-field modeling of the interactions between an edge dislocation and an array of obstacles, Comput. Methods Appl. Mech. Eng. 389 (2022) 114426.

[48] Z. Li, J.Y. Cheng, J.D. Poplawsky, S. Xu, J.K. Baldwin, I.J. Beyerlein, N.A. Mara, Critical length scales for chemical heterogeneity at Cu/Nb 3D interfaces by atom probe tomography, Scr. Mater. 223 (2023) 115078.

[49] S. Xu, J.Y. Cheng, N.A. Mara, I.J. Beyerlein, Dislocation dynamics in heterogeneous nanostructured materials, J. Mech. Phys. Solids 168 (2022) 105031.

[50] S. Xu, J.Y. Cheng, N.A. Mara, I.J. Beyerlein, Thick interface size effect on dislocation transmission in nanolaminates, IOP Conf. Ser. Mater. Sci. Eng. 1249 (2022) 012005.

[51] J.Y. Cheng, S. Xu, Y. Chen, Z. Li, J.K. Baldwin, I.J. Beyerlein, N.A. Mara, Simultaneous high-strength and deformable nanolaminates with thick biphase interfaces, Nano Lett. 22 (2022) 1897–1904.

[52] N. Li, J. Wang, A. Misra, J.Y. Huang, Direct observations of confined layer slip in Cu/Nb multilayers, Microsc. Microanal. 18 (2012) 1155–1162.

[53] J. Wang, M. Knezevic, M. Jain, S. Pathak, I.J. Beyerlein, Role of interface-affected dislocation motion on the strength of Mg/Nb nanolayered composites inferred by dual-mode confined layer slip crystal plasticity, J. Mech. Phys. Solids 152 (2021) 104421.

[54] M.D. Uchic, P.A. Shade, D.M. Dimiduk, Plasticity of micrometer-scale single crystals in compression, Annu. Rev. Mater. Res. 39 (2009) 361–386.

[55] F. Bachmann, R. Hielscher, H. Schaeben, Texture analysis with MTEX- Free and open source software toolbox, Solid State Phenom. 160 (2010) 63–68.

[56] B.B. He, Two-Dimensional X-Ray Diffraction, John Wiley & Sons, 2018.

[57] J.M. Cairney, P.R. Munroe, Redeposition effects in transmission electron microscopy specimens of FeAl-WC composites prepared using a focused ion beam, Micron 34 (2003) 97–107.

[58] W.F. Hosford, Mechanical Behavior of Materials, Cambridge University Press, 2010.

[59] Y. Liang, A. Luo, L. Yang, J. Zhao, L. Wang, Q. Wan, Effect of interface structure and layer thickness on the mechanical properties and deformation behavior of Cu/Ag nanolaminates, Phys. B Condens. Matter 661 (2023) 414933.

[60] R. Su, D. Neffati, J. Cho, Z. Shang, Y. Zhang, J. Ding, Q. Li, S. Xue, H. Wang, Y. Kulkarni, X. Zhang, High-strength nanocrystalline intermetallics with room temperature deformability enabled by nanometer thick grain boundaries, Sci. Adv. 7 (2021) 1–9.

[61] N. Li, N.A. Mara, J. Wang, P. Dickerson, J.Y. Huang, A. Misra, *Ex situ* and *in situ* measurements of the shear strength of interfaces in metallic multilayers, Scr. Mater. 67 (2012) 479–482.

[62] J. Wang, R.G. Hoagland, X.Y. Liu, A. Misra, The influence of interface shear strength on the glide dislocation- interface interactions, Acta Mater. 59 (2011) 3164–3173.

[63] J. Wang, R.G. Hoagland, A. Misra, Mechanics of nanoscale metallic multilayers: From atomic-scale to micro-scale, Scr. Mater. 60 (2009) 1067–1072.

[64] Z.C. Cordero, B.E. Knight, C.A. Schuh, Six decades of the Hall–Petch effect – a survey of grain-size strengthening studies on pure metals, Int. Mater. Rev. 61 (2016) 495–512.

[65] N.L. Okamoto, D. Kashioka, T. Hirato, H. Inui, Specimen- and grain-size dependence of compression deformation behavior in nanocrystalline copper, Int. J. Plast. 56 (2014) 173–183.

[66] H. Zhang, B.E. Schuster, Q. Wei, K.T. Ramesh, The design of accurate micro-compression experiments, Scr. Mater. 54 (2006) 181–186.

[67] C. Zener, Elasticity and Anelasticity of Metals, University of Chicago Press, 1965.

[68] Y. Su, M. Ardeljan, M. Knezevic, M. Jain, S. Pathak, I.J. Beyerlein, Elastic constants of pure body-centered cubic Mg in nanolaminates, Comput. Mater. Sci. 174 (2020) 109501.

[69] T. Chen, R. Yuan, I.J. Beyerlein, C. Zhou, Predicting the size scaling in strength of nanolayered materials by a discrete slip crystal plasticity model, Int. J. Plast. 124 (2020) 247–260.

[70] S. Huang, I.J. Beyerlein, C. Zhou, Nanograin size effects on the strength of biphase nanolayered composites, Sci. Rep. 7 (2017) 1–10.

[71] Y. Shen, P.M. Anderson, Transmission of a screw dislocation across a coherent, slipping interface, Acta Mater. 54 (2006) 3941–3951.

[72] J. Wang, R.G. Hoagland, J.P. Hirth, A. Misra, Atomistic modeling of the interaction of glide dislocations with "weak" interfaces, Acta Mater. 56 (2008) 5685–5693.

[73] M.J. Demkowicz, R.G. Hoagland, Structure of Kurdjumov-Sachs interfaces in simulations of a copper-niobium bilayer, J. Nucl. Mater. 372 (2008) 45–52.

[74] Altman, Y., export_fig (https://github.com/altmany/export_fig/releases/tag/v3.42), GitHub (2023).